Contribution of the Southern Annular Mode on variations in water isotopes of daily precipitation at Dome Fuji, East Antarctica

Kanon Kino[1,1], Atsushi Okazaki[2,2], Alexandre Cauquoin[3,3], and Kei Yoshimura[4,4]

[1]Atmosphere and Ocean Research Institute, The University of Tokyo
[2]Pennsylvania State University
[3]Institute of Industrial Science, The University of Tokyo
[4]University of Tokyo

November 30, 2022

Abstract

Water isotopes measured in Antarctic ice cores allow reconstruction at the first order of the past temperature variations. However, the seasonality of the precipitation and episodic events including synoptic-scale disturbances influence the isotopic signals recorded in ice cores. This study adopted an isotope-enabled atmospheric general circulation model for the period from 1981 to 2010 to investigate variations in climatic factors in $\delta^{18}O$ of precipitation ($\delta^{18}O_p$) at Dome Fuji, East Antarctica. The results show that the Southern Annular Mode (SAM), the primary mode of atmospheric circulation in the southern mid-high latitudes, significantly contributes to the isotope signals. Positive $\delta^{18}O_p$ anomalies, especially in the austral winter, are linked to the negative polarity of the SAM, which weakens westerly winds and increases the southward inflow of water vapor flux. Daily variations in temperature and $\delta^{18}O_p$ in Dome Fuji are significantly small in the austral summer, and their contribution to the annual signals is limited. It is also suggested that the isotope signals driven by the SAM are a locational feature of Dome Fuji, related to the asymmetric component of the SAM.

K. Kino[1,2], A. Okazaki[3], A. Cauquoin[2], and K. Yoshimura[2]

[1]Atmosphere and Ocean Research Institute, The University of Tokyo, Kashiwa, Japan

[2]Institute of Industrial Science, The University of Tokyo, Kashiwa, Japan

[3]Hirosaki University, Hirosaki, Japan

Corresponding author: Kanon Kino (kanon@aori.u-tokyo.ac.jp)

Key Points:

- An isotope-enabled climate model successfully reproduces the observed daily variations in precipitated stable oxygen isotopes at Dome Fuji.
- The negative polarity of the Southern Annular Mode allows moisture flux with heavy oxygen isotopes to flow from the north around Dome Fuji.
- This polarity contributes to precipitate heavy isotopes at Dome Fuji as a locational feature related to the mode's asymmetric component.
-

Abstract

Water isotopes measured in Antarctic ice cores allow reconstruction at the first order of the past temperature variations. However, the seasonality of the precipitation and episodic events including synoptic-scale disturbances influence the isotopic signals recorded in ice cores. This study adopted an isotope-enabled atmospheric general circulation model for the period from 1981 to 2010 to investigate variations in climatic factors in ^{18}O of precipitation ($^{18}O_p$) at Dome Fuji, East Antarctica. The results show that the Southern Annular Mode (SAM), the primary mode of atmospheric circulation in the southern mid-high latitudes, significantly contributes to the isotope signals. Positive $^{18}O_p$ anomalies, especially in the austral winter, are linked to the negative polarity of the SAM, which weakens westerly winds and increases the southward inflow of water vapor flux. Daily variations in temperature and $^{18}O_p$ in Dome Fuji are significantly small in the austral summer, and their contribution to the annual signals is limited. It is also suggested that the isotope signals driven by the SAM are a locational feature of Dome Fuji, related to the asymmetric component of the SAM.

Plain language summary

This study employs a climate model including water isotopes to investigate how water isotopic components in snowfall precipitation, such as $^{18}O_p$, are determined at Dome Fuji, East Antarctica. Results show that the primary mode of atmospheric circulation in the southern mid-high latitudes (SAM) is significantly associated with daily $^{18}O_p$ signals, particularly in the austral winter. The negative polarity of the SAM weakens westerly winds, increases the inflow from the north to Dome Fuji, and induces large snowfalls that accompany warming. Moreover, SAM affects the $^{18}O_p$ clear shift compared with the local surface

air temperature. Thus, it contributes to the warm bias in the accumulated snow due to the lack of cold days. We also demonstrate that this is a locational feature of Dome Fuji. Our results indicate that the $^{18}O_p$ in Antarctica is complexly determined by the global dynamical circulation of the atmosphere and water cycles. Hence, it is important to consider the recording processes of isotopic proxies for the interpretation of water isotope records considering past climate variations.

1 Introduction

Stable isotopes of water ($H_2{}^{16}O$, $H_2{}^{18}O$, and $HD^{16}O$) have been successfully used during the last decades for studying past climate variations on Earth, particularly for the period before the instrumental era, when no direct measurements existed. The water isotopes of deep ice cores from inland sites of East Antarctica have provided continuous information on climate changes for the last 800,000 years (Dome Fuji Ice Core Project Members et al., 2017; Jouzel et al., 2007) with the potential to expand these records beyond one million years (Fischer et al., 2013; Karlsson et al., 2018). Thanks to the first order linear relationship between annual mean air temperatures and the ratio of stable water isotopes (D/H and $^{18}O/^{16}O$; expressed hereafter in the usual notation ^{2}H and ^{18}O, with respect to the Vienna Standard Mean Ocean Water V-SMOW) in snow and ice (Dahe et al., 1994; Dansgaard, 1964; Satow et al., 1999), water isotopes have been widely used as proxies for past temperature changes.

However, the interpretation of changes in water isotope contents in terms of temperature variations remains a subject of debate and requires continued investigation (Buizert et al., 2014, 2021; Cauquoin et al., 2015; Jouzel, 1999; Sime et al., 2009; Werner et al., 2016). It is accepted that water isotopes reflect precipitation-weighted mean signals rather than the annual mean (Krinner & Werner, 2003; Sime et al., 2011; Werner et al., 2018). Seasonal variations in precipitation (Erb et al., 2018; Laepple et al., 2011; Noone & Simmonds, 1998; Schlosser, 1999; Sime & Wolff, 2011; Steig et al., 1994; Werner et al., 2001) and synoptic-scale disturbances (Dittmann et al., 2016; Fujita & Abe, 2006; Hirasawa et al., 2000, 2013; Schlosser et al., 2010; 2017; Stenni et al., 2016; Turner et al., 2019) have also been suggested to contribute to water isotope signals. Several paleoclimate modeling studies proposed that the recorded signals of Antarctic ice cores were weighted toward austral winter (Erb et al., 2018; Laepple et al., 2011; Sime & Wolff, 2011), while Antarctic precipitation is poorly constrained due to the lack of direct observations (Marshall et al., 2017; Turner et al., 2019) and less certainty in the general circulation model (GCM) results (Sime & Wolf, 2011). Other studies suggest that the precipitation processes related to the atmospheric circulation modified accumulated water isotope signals (Cole et al., 1999; Noone & Simmonds, 1998). Precipitation in Antarctica does not only comprise clear-sky precipitation (or diamond dust) but also episodically caused by synoptic disturbances (Hirasawa et al., 2000, 2013; Schlosser et al., 2010; Turner et al., 2019). Most disturbances are accompanied by amplified Rossby waves, which lead to the southward advection of warm and moist air

from relatively low latitudes (Schlosser et al., 2010). Although the synoptic disturbances have less impact inland compared with coastal regions, the accompanying episodic precipitation events comprise the largest 10% of daily totals, which contribute to approximately 40% of the total annual precipitation in inland East Antarctic regions (Turner et al., 2019). Abrupt changes in isotopic values with such episodic events are supported by annual *in-situ* observations at a few ice core sites (Fujita & Abe, 2006; Stenni et al., 2016). Following precise classification, the water isotope signals at the sites can differ significantly among synoptic weather patterns (Dittmann et al., 2016; Schlosser et al., 2017). However, the limitation of observation periods for the isotope signals prevented us from investigating deeper statistical analyses (Schlosser et al., 2017).

Isotope-enabled versions of atmospheric GCMs (AGCMs) are useful to obtain a systematic understanding of how isotopes record climate (Yoshimura, 2015). One of the advantages of using such AGCMs is their ability to explicitly calculate both dynamical circulations and water transport in the atmosphere, including the water isotope diagnostics. Early studies using such an AGCM showed that a large fraction of the isotope signals from inland regions of East Antarctica were dynamically linked to the Southern Annular Mode (SAM) by affecting the condensation history of parcels and the location of the water vapor source region (Noone & Simmonds, 2002; Noone, 2008). SAM is a principal atmospheric mode in the mid-high latitudes of the southern hemisphere. Other studies have also suggested that the polarity of the SAM could be important for the interpretation of the ice core proxies because westerly winds intensified by the positive polarity of the SAM serve to isolate the main Antarctic continent from the southward heat advection by synoptic disturbances (Marshall et al., 2011; Masson-Delmotte et al., 2011; Schlosser et al., 2016). Although the SAM is generally defined as a monthly index, recent studies demonstrated that it also makes a robust contribution to daily variations in surface air temperature (SAT) and precipitation of most of Antarctica (Marshall et al., 2017; Marshall & Thompson, 2016; Thompson & Woodworth, 2014).

In this study, the contribution of the atmospheric circulation, specifically the SAM, to variations in ^{18}O of precipitation (hereafter $^{18}O_p$) at Dome Fuji in East Antarctica was investigated using an isotope-enabled AGCM MIROC5-iso (Okazaki & Yoshimura, 2019). A simulation was conducted for the period from 1981 to 2010 and nudged toward JRA-25 reanalysis fields (Onogi et al., 2007). The remainder of this paper is organized as follows. In Section 2, we describe the model, experimental design, observational dataset, and analysis methods. In Section 3, the simulated results are evaluated with observations. In Section 4, the linkage of daily variations in $^{18}O_p$ at Dome Fuji with the changes in SAT, precipitation, and atmospheric vapor concentration is statistically analyzed. In section 5, the influence of SAM on the entire Antarctic surface climate and $^{18}O_p$ at Dome Fuji are discussed. Further discussions and conclusions are presented in Section 6.

2 Methods

2.1 Atmospheric Model

The atmospheric component of the fifth version of the Model for Interdisciplinary Research on Climate (MIROC5; Watanabe et al., 2010) is based on a three-dimensional primitive equation in the hybrid -p coordinate, with a spectral truncation adopted for horizontal discretization. The physical parameterizations adopted are: Chikira scheme (Chikira, 2014; Chikira & Sugiyama, 2010) for cumulus convection; the large-scale condensation scheme (Watanabe et al., 2009); the bulk microphysical scheme (Wilson & Ballard, 1999); the two-stream k-distribution scheme (Nakajima et al., 1986; Sekiguchi & Nakajima, 2008) for radiation; and Mellor–Yamada–Nakanishi–Niino's level 2.5 closure scheme (Mellor & Yamada, 1974, 1982; Nakanishi, 2001; Nakanishi & Niino, 2004) for vertical mixing. For the land surface component, an independent model named Minimal Advanced Treatment of Surface Interaction and RunOff (Takata et al., 2003) is used.

The implementation of water isotopes in the atmosphere and land surface parts of MIROC5 has been described in detail by (Okazaki & Yoshimura, 2019), and this model version has been labeled as MIROC5-iso. Most fractionations in phase transitions are assumed to occur at thermodynamic equilibrium (Jouzel et al., 1987). However, kinetic fractionation occurs at surface evaporation from open water (Merlivat & Jouzel, 1979), condensation from vapor to ice under supersaturation conditions (Jouzel et al., 1987), and evaporation and isotopic exchange from liquid raindrops into unsaturated air (Stewart, 1975; Yoshimura et al., 2008). The implementation of isotopes in cloud microphysics is based on (Federer et al., 1982) and (Blossey et al., 2010). For phase changes occurring at any type of surface in the model, equilibrium and kinetic fractionations are considered (Yoshimura et al., 2006).

2.2 Model Setup and Experimental Design

We conducted a simulation for the period from1981 to 2010 following the design of Okazaki and Yoshimura (2019). The resolution of MIROC5-iso is set to a horizontal spectral truncation of T42 (approximately 280 km) and 40 vertical layers with a -p hybrid coordinate. Sea surface temperature and sea ice concentration (HadISST; Rayner, 2003), greenhouse gases (carbon dioxide, methane, and chlorofluorocarbons), ozone, and land-use changes were given as external forcings, following the experimental design proposed by the fifth phase of the climate model intercomparison project for historical runs (Taylor et al., 2012). For the isotopic boundary conditions, isotopic compositions of the surface seawater and lake water (0‰), and sea ice (3‰; Joussaume & Jouzel, 1993) were assumed to be constant over time. The horizontal wind velocity was nudged toward the Japanese 25-year reanalysis fields (Onogi et al., 2007). The simulation was initiated after the year 1980 of Okazaki and Yoshimura (2019) to extract daily mean variables and was completed in 2010, which is the last year of JRA-25.

2.3 Isotopic Observation Data

To evaluate simulated daily SAT, precipitation, and $^{18}O_p$ at Dome Fuji in Antarctica, we used observations from 3 February 2003 to 20 January 2004 by (Fujita & Abe, 2006), who were the first to perform direct precipitation measurements and sampling for isotopic measurements in central Antarctica. The advantages of direct precipitation measurements compared to accumulation measurements are that wind scouring and sublimation after the snowfall are reduced to a minimum. The water isotopes of the precipitation samples are also not affected by post-depositional processes, such as exchange with the atmosphere at the snow-air interface or diffusion within the snowpack/ice. This is described in detailed by Fujita & Abe (2006) and Dittmann et al. (2016).

2.4 Analysis Methods for Simulation Results

For daily SAT and $^{18}O_p$, deviations from daily climatology for the period from 1981 to 2010 were used in Sections 4 and 5. Monthly and annual $^{18}O_p$ values were obtained by weighting daily $^{18}O_p$ with the precipitation amount. Days of positive and negative anomalies of $^{18}O_p$ at Dome Fuji (hereafter $^{+}$ and $^{-}$) were defined when the anomalous values were greater than +1 standard deviation (noted after) or less than -1 , respectively. These thresholds were defined arbitrarily; note, they did not affect the interpretation of the results if a threshold of 0 or ±0.5 was chosen instead.

The atmospheric pattern of the SAM was calculated as a leading empirical orthogonal function (EOF) of the anomalous monthly mean of 500 hPa geopotential height between latitudes 20–90°S for the period from 1981 to 2010, based on the definition by (Marshall & Thompson, 2016). A daily mean expansion coefficient time series of the SAM (SAM index) was deduced by projecting an anomalous daily mean of 500 hPa geopotential height onto the resulting EOF pattern as in (Marshall & Thompson, 2016). Climate Data Operators (Schulzweida, 2019) was used for these calculations. The resulting daily time series was standardized to mean = 0 and =1 a standard deviation of one. Days in the positive and negative modes of the SAM (hereafter SAM^+ and SAM^-) were defined when the index values were greater than +1 and less than –1, respectively.

3 Evaluation of MIROC5-iso at Dome Fuji

MIROC5-iso simulates consistently the $^{18}O_p$ distribution at the global scale, as already shown by (Okazaki & Yoshimura, 2019) and confirmed in Figure S1 for our experiment design. We focus here on the evaluation of our simulated daily mean variations of SAT, precipitation, and $^{18}O_p$ by comparing them with the observations from (Fujita & Abe, 2006), over the period from February 2003 to January 2004 (Figure 1). Simulated and observed averages for the observation period were comparable for both the precipitation rate (25.2 mm of simulated equivalent water (w.e.) and 27.5 mm w.e. in the observations) and the $^{18}O_p$ (−57.5 ‰ and −58.7 ‰, respectively), while a warm bias existed in the model SAT (-50.9 °C in the simulation against -54.7 °C in the observations). This bias, frequent in AGCM simulations (Masson-Delmotte et al., 2006), could be linked to the general poor representation of the polar atmospheric boundary

layer and related atmospheric inversion temperatures in these models (Krinner et al., 1997). Too many high clouds, generally seen in CMIP5 models and giving stronger downwelling longwave radiation, can also partially account for the overestimation of temperatures in Antarctica (Cauquoin et al., 2019a; Cesana & Chepfer, 2012).

In Figure 1a, $^{18}O_p$ shows a well-known seasonality, i.e., higher values in the warmer season and lower values in the colder season (e.g., Motoyama, 2005). The range of modeled $^{18}O_p$ (difference of maximum and minimum in Figure 1a) was 105.2 ‰, which was 2.1 times larger than the observed one. The range of modeled SAT in the same context was 65.6 °C, which was 1.4 times larger than the observed range. Nevertheless, most patterns of modeled daily variations of $^{18}O_p$ and SAT agreed with the observations (r (Spearman's correlation coefficient) = 0.89 for SAT, and r = 0.82 for $^{18}O_p$). According to the observations, these increases accompanied precipitation events. This pattern was well reproduced in our simulation, with the exception of some days in January, in which MIROC5-iso overestimated the amount of precipitation and underestimated the variability of SAT and $^{18}O_p$ (Figure 1). This may also be a part of the frequent bias in AGCM simulations. The typical synoptic weather patterns (e.g., an amplified high-pressure ridge on 1 August 2003) proposed by (Dittmann et al., 2016) were also confirmed in our simulation results (data not shown). These analyses confirm that MIROC5-iso is sufficiently suitable to investigate the daily $^{18}O_p$ variations at Dome Fuji.

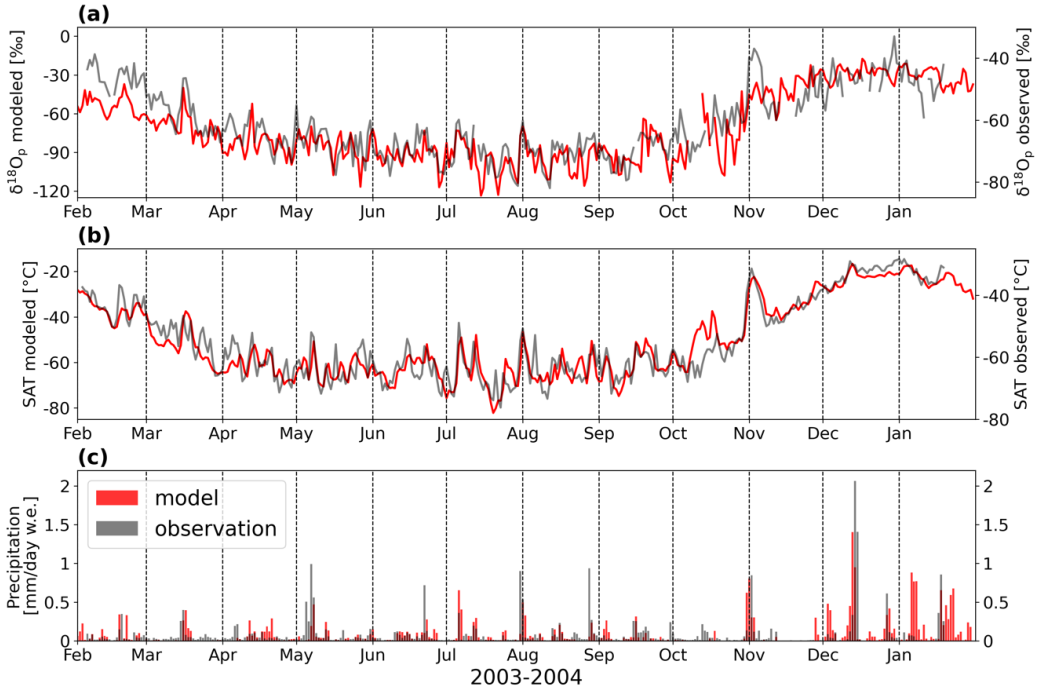

Figure 1 Seasonal changes in simulated (red; left y-axes) and observed (black; right y-axes; (Fujita & Abe, 2006) in **a** $^{18}O_p$, **b** surface air temperature, and **c** daily mean precipitation in water equivalent at Dome Fuji from February 2003 to January 2004.

4 Influence of the SAM on daily variations in $^{18}O_p$ at Dome Fuji

Statistical analyses for the period from 1981 to 2010 were conducted to consider the climatic driver of daily $^{18}O_p$ variations. The modeled SAT and precipitation were positively correlated with $^{18}O_p$ during the austral winter (from March to October; Figure 2 and Table S1), suggesting that the well-known temperature effect was dominant in determining $^{18}O_p$ during those months. Meanwhile, there was little temperature effect in $^{18}O_p$ during the austral summer (from November to February), which contradicts the observations (Table S2). Observed SAT and $^{18}O_p$ showed similar seasonality in the magnitude of the variabilities (Figure 1): large in the austral winter; small in the austral summer. These characteristics were well simulated by MIROC5-iso for the period from 1981 to 2010: standard deviations of SAT ($^{18}O_p$) from April to September (from May to October) were larger than the annual value (Figure 3 and Table S3).

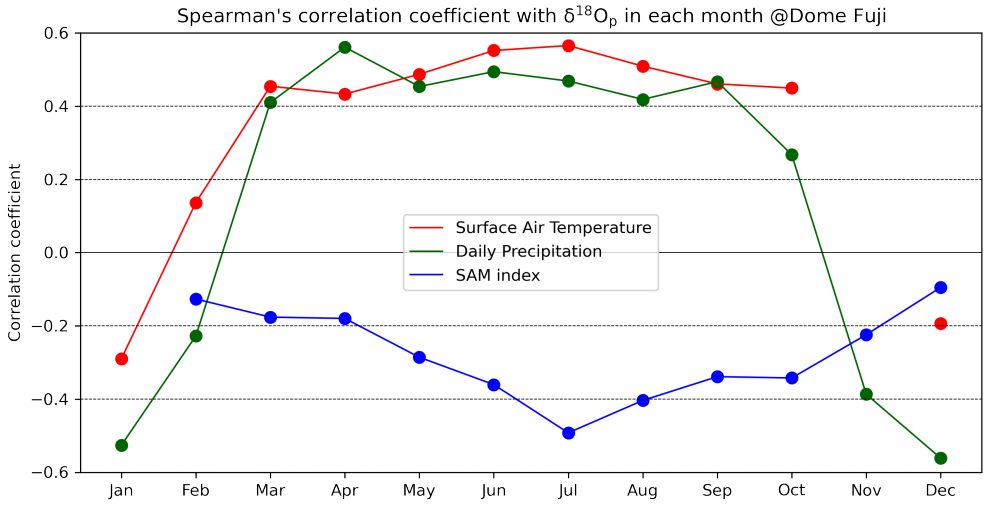

Figure 2 Spearman's correlation coefficient between modeled daily $^{18}O_p$ and surface air temperature (red), precipitation (green), and SAM index (blue) in each month for the whole period from 1981 to 2010. Only correlation coefficients with p-values lower than 0.05 are shown. All values are listed in Table S1.

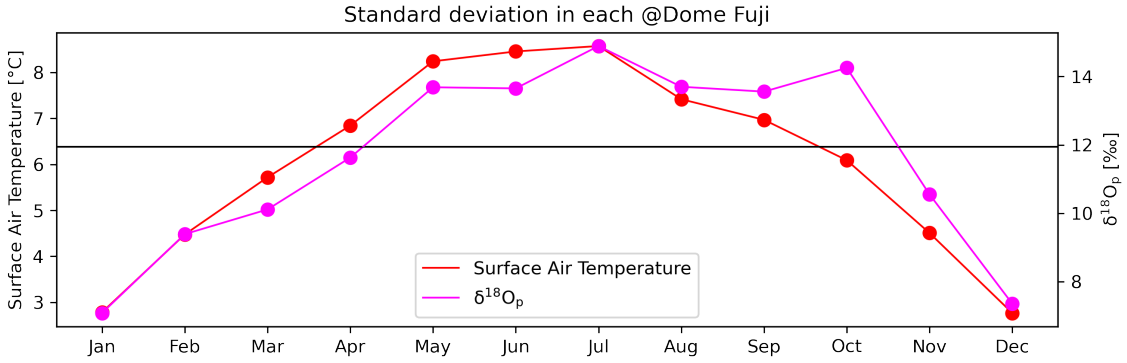

Figure 3 Standard deviations of modeled daily SAT (red) and $^{18}O_p$ (magenta) in each month for the whole period from 1981 to 2010. The standard deviation for the entire year of SAT and $^{18}O_p$ are commonly presented as a horizontal black line. All values are listed in Table S3.

The difference in the composites of geopotential height at 500 hPa level between $^{+}$ and $^{-}$ (days of positive and negative anomalies of $^{18}O_p$ at Dome Fuji; see Section 2.3) for the entire year (Figure 4a) was quite similar to that in the austral winter (Figure 4b), whereas the pattern in the austral summer was unclear (Figure 4c). These results suggest minimal influence of the signals in

the austral summer on the annual states. These atmospheric circulation patterns exhibited planetary-scale wave patterns, similar to the well-known structure of the SAM (Figure 4e), i.e., low pressure covering Antarctica surrounded by three high-pressure areas. The wavenumber 3 pattern around Antarctica, which is an asymmetric component of the SAM and a dominant feature of the daily circulation of the atmosphere (Fogt et al. 2012; Raphael 2004; 2007), alters the longitudinal patterns of northward and southward advection (Fogt and Marshall, 2020). The composites of the atmospheric pattern for $^{18}O_p$ ($^+$ minus $^-$) from June to August (JJA) (Figure 4d) presented clearer three low pressures, similar to the SAM pattern. Thus, the SAM index was negatively correlated with the $^{18}O_p$ in the austral winter and especially strong in JJA (less than -0.36 in Table S1).

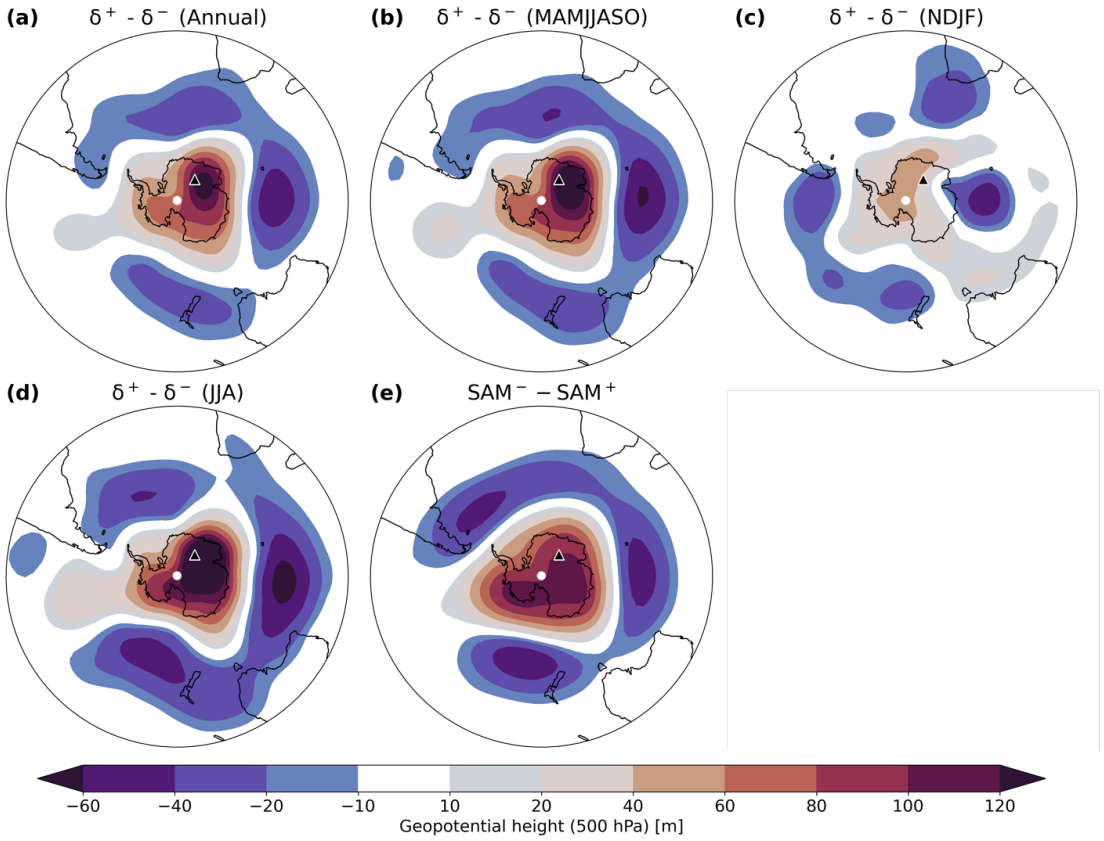

Figure 4 Difference in simulated geopotential height at 500 hPa for the whole period from 1981 to 2010 between $^+$ and $^-$: **a** for the entire year, **b** for the months from March to October, **c** from November to February and **d** from June to August. **e** Same as **a** but in SAM$^-$ and SAM$^+$. For **a**-**e**, the location of Dome

Fuji is plotted as a triangle.

The strong association between the SAM and $^{18}O_p$ at Dome Fuji in JJA was also confirmed by moisture flow. That is, the difference in composites of vertically integrated moisture fluxes between $^{+}$ and $^{-}$ in JJA represented a penetration of moisture fluxes from the north to around Dome Fuji (dashed contours in Figure 5a). This was similar to the pattern in SAM^{-} minus SAM^{+} (dashed contours in Figure 5b), suggesting that $^{18}O_p$ signals at Dome Fuji were ultimately driven by the zonal wavenumber 3 pattern, namely the SAM. The distribution of ^{18}O in the atmospheric vapor (hereafter $^{18}O_v$) also exhibited similar patterns (colors in Figures 5a and 5b), with strong increases around Dome Fuji (more than +10 ‰), decreases surrounding Antarctica except for an upper stream of Dome Fuji (approximately -1 ‰), and slight increases in the three regions over the ocean (approximately +1 ‰), corresponding to the three low pressure areas in Figures 4d and 4e. We concluded that the transport of water vapor with heavier $^{18}O_v$ from the southern Atlantic Ocean to Dome Fuji was prominent both in $^{+}$ minus $^{-}$ and SAM^{-} minus SAM^{+}, contributing with the heavy $^{18}O_p$ at the ice core site. The inter-annual time series of $^{18}O_p$ and SAM index, i.e. their 12-month moving averages, shown in Figure 6 were significantly correlated with the period from 1981 to 2010 ($r = 0.43$, $p < 0.01$), confirming that $^{18}O_p$ to serves as an indicator of SAM index. Although the influence of SAM on $^{18}O_p$ at Dome Fuji was moderate or limited in the austral summer (Figure 2 and Table S1), the SAM in the austral winter significantly contributed to determining the annual states of $^{18}O_p$.

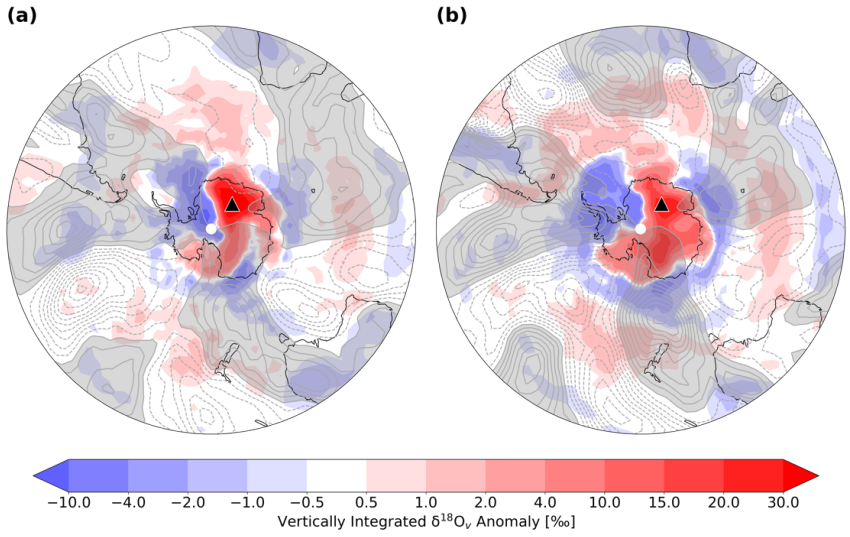

Figure 5 **a** Differences in simulated vertically integrated $^{18}O_v$ (colors) and simulated meridional moisture flux in JJA between $^{+}$ and $^{-}$ (contours); **b** Same as **a** but for SAM^{-} and SAM^{+}. For **a** and **b**, contours are drawn in every 5 g/kg • m/s; northward flux in solid lines with gray shades; and southward flux in dashed lines; the location of Dome Fuji is plotted as a triangle.

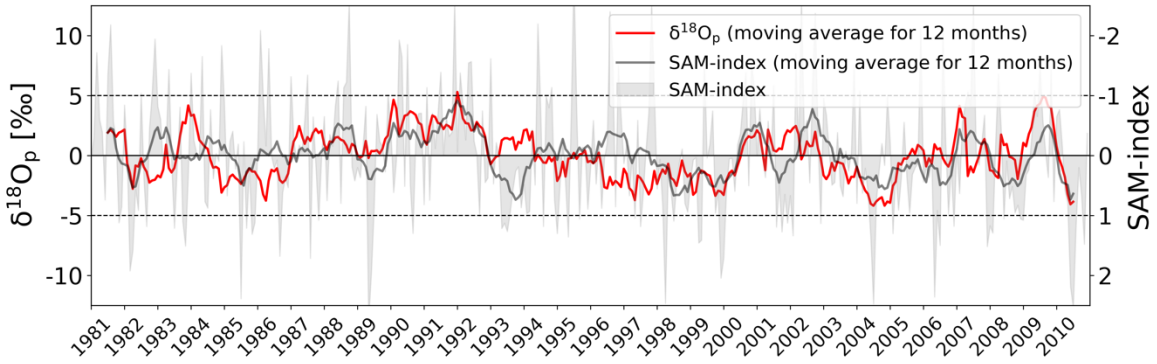

Figure 6 Inter-annual time series of simulated $^{18}O_p$ at Dome Fuji (red) and simulated SAM index (dark gray) for the period from 1981 to 2010. The inter-annual time series for each variable are calculated as 12-month moving averages. $^{18}O_p$ is shown as an anomaly from its annual climatology after weighting by daily mean precipitation. The simulated monthly defined SAM index is also shown as gray shades.

5 Influence of the Southern Annular Mode on $^{18}O_p$ at Dome Fuji

Figure 7 shows the effects of the SAM on daily SAT, precipitation, and $^{18}O_p$ in the southern high latitudes during JJA. Spatial distributions of differences in modeled SAT and precipitation between SAM^{-} and SAM^{+} (Figures 7a and 7b) agreed with the results on the European Centre for Medium Range Weather Forecasts ERA-Interim reanalysis (Marshall et al., 2017; Marshall & Thompson, 2016). SAM^{-} presented an increase in SAT in Antarctica, except for the western peninsula (Figure 7a). The differences were large on the east of Dome Fuji and Ross ice shelf (+9.3 °C in Dome Fuji). In SAM^{-} days, the amount of precipitation was lower in the Atlantic sector and enhanced in the remaining regions (Figure 7b). The maxima precipitation anomaly (more than 200 %) were on the west of the SAT anomaly maxima region, which reflected the larger lapse rate with drier conditions in the lower stream. SAM^{-} days came with higher $^{18}O_p$ in most of Antarctica. The maxima $^{18}O_p$ anomaly appeared in the inland East Antarctic region (Figure 7c), which was close to the location of maxima of SAT and precipitation anomalies. Finally, Dome Fuji is positioned in a region where the effect of SAM on surface climate is especially strong (+20.3‰ on $^{18}O_p$ at Dome Fuji). It may correspond to the third mode described by (Schneider et al., 2004), related to the blocking event reported by (Hirasawa et

al., 2000).

The scatterplot and histograms of simulated SAT and $^{18}O_p$ for SAM$^-$ days (red) and SAM$^+$ days (blue) at Dome Fuji in JJA are shown in Figure 8, as well as the corresponding $^{18}O_p$/SAT relationships. SAM$^+$ significantly increased SAT and $^{18}O_p$, whereas SAM$^-$ had the opposite effect. While the linear regression lines of the $^{18}O_p$/SAT for SAM$^-$ and SAM$^+$ days were mostly parallel (0.89 ‰°C^{-1} and 0.80 ‰°C $^{-1}$, respectively), a strong shift of 10.5 ‰ between the two ensembles was observed. This shift reflected the contribution of the SAM to $^{18}O_p$/SAT relationships described in Section 4; in SAM$^-$ days, the mean $^{18}O_v$ around Dome Fuji was increased by enhancing the moisture flux with heavier $^{18}O_v$ coming from the north (Figure 5b). Moreover, precipitation was mostly in favor of SAM$^-$ days compared with SAM$^+$ days (2.85 mm w.e. and 0.63 mm w.e. for respective maxima of daily mean precipitation; Figure 8). Hence, the influence of SAM was represented in the inter-annual time series of $^{18}O_p$ (Figure 6), and was also expected for ^{18}O in accumulated snow/ice.

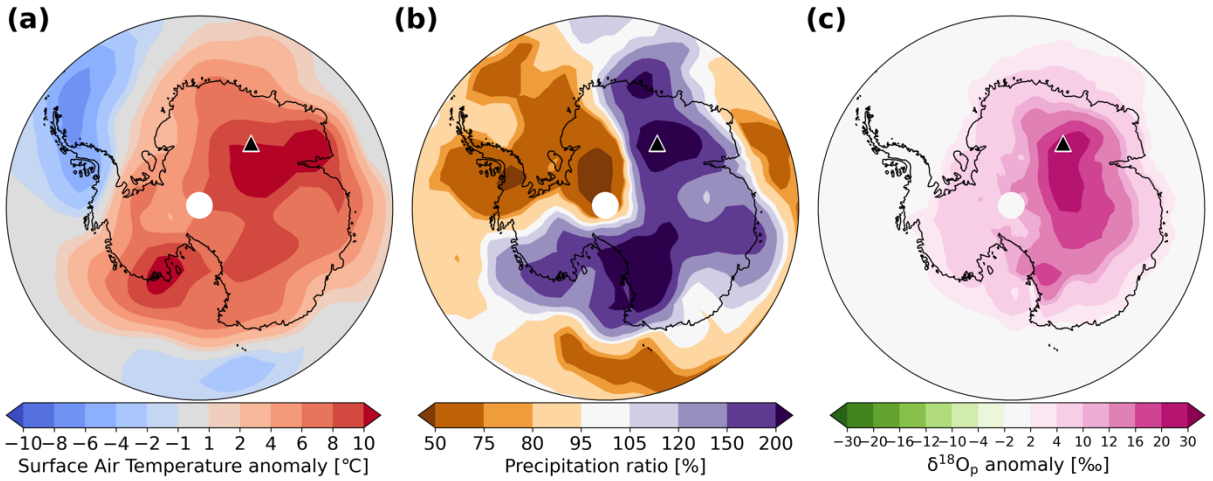

Figure 7 Differences in simulated **a** SAT, **b** precipitation, and **c** $^{18}O_p$ weighted by daily mean precipitation in JJA between SAM$^-$ and SAM$^+$. For **b**, the differences are shown in the ratio (SAM$^-$/SAM$^+$). For **a, b,** and **c**, the location of Dome Fuji is plotted as a triangle.

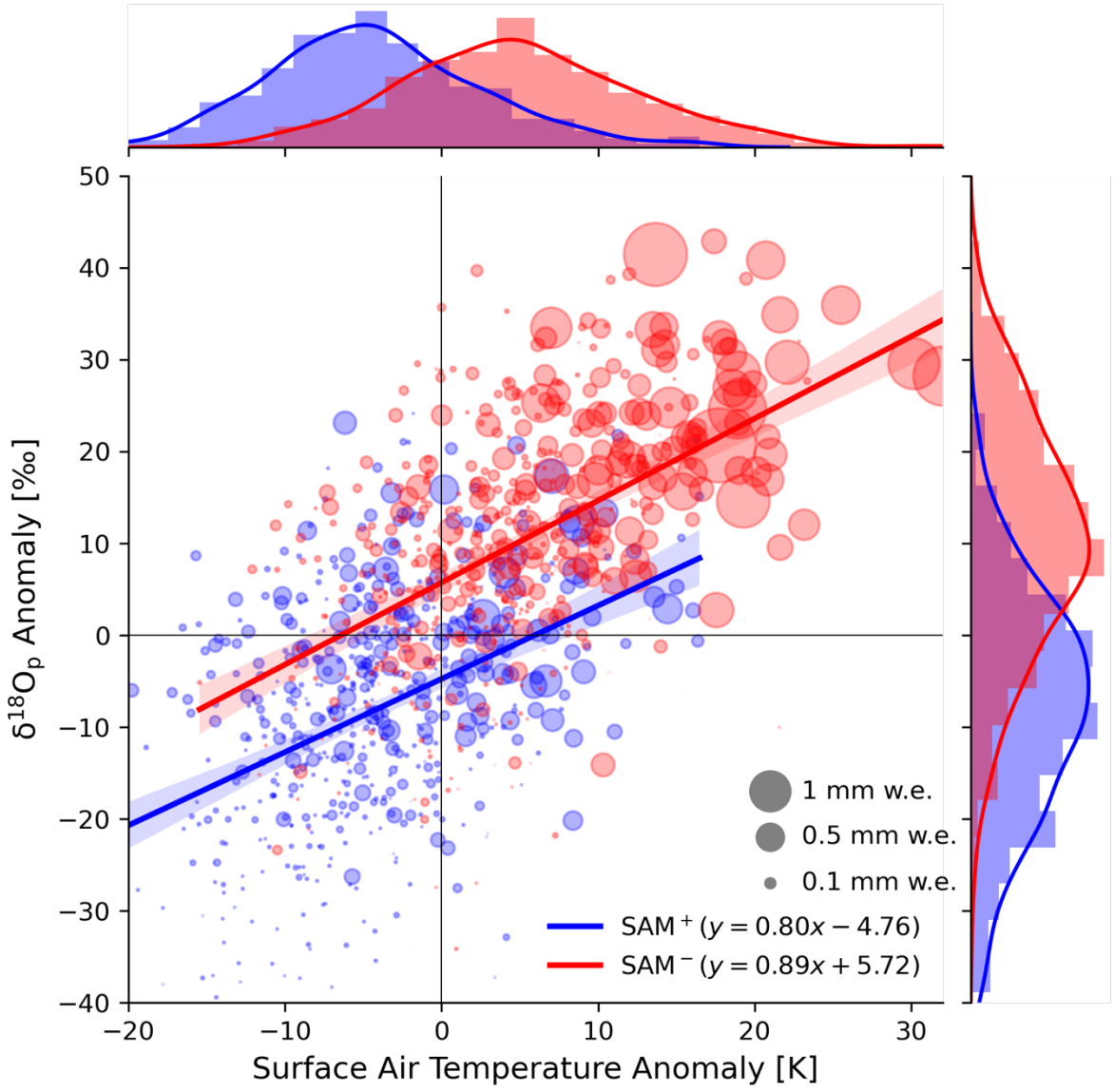

Figure 8 Cross plot of daily surface air temperature vs. $^{18}O_p$ with their histograms in SAM$^+$ (blue) and SAM$^-$ (red) days of JJA at Dome Fuji. Each value is an anomaly from the respective daily climatology. The size of each bubble corresponds to daily mean precipitation (gray bubbles in the bottom right show the legends). Linear regression lines of SAM$^+$ and SAM$^-$ are drawn with 95 % confidence intervals (shades), and the corresponding equations are given in the legends.

6 Discussions and conclusions

This study investigated the contribution of large-scale atmospheric circulation to the isotope signals at Dome Fuji in East Antarctica using MIROC5-iso. The daily variations in $^{18}O_p$ at Dome Fuji were well reproduced by our model and were revealed to be significantly affected by the SAM, which is the principal atmospheric mode in the mid-high latitudes of the southern hemisphere. Its influence on the water isotope signal was observed, especially in the austral winter. When SAM was in the negative phase, $^{18}O_p$ mostly increased due to the westerly wind being stagnated to the north of Dome Fuji over the Southern Ocean, and the southward water vapor flux toward the Dome Fuji being increased. In the positive phase of SAM, the intensified westerly winds isolated the continent from southward heat advection. Finally, the polarity of the SAM systematically shifted the linear relationship of $^{18}O_p$/SAT and contributed to the inter-annual variations of $^{18}O_p$. SAM^+ days during austral winter, which are generally colder and drier, were not necessarily recorded in Dome Fuji ice core, in agreement with a recent study using virtual ice cores (Casado et al., 2020). The polarity of the SAM contributed to a warm and isotopically enriched bias in the accumulated snow at Dome Fuji.

Our results show the SAM impacts on not only seasonal or annual mean precipitation but also the incidence of extreme precipitation events at Dome Fuji in the austral winter. This supports (Marshall et al., 2017), who provided a detailed analysis of the contributions of major patterns of large-scale southern hemisphere circulation (including the SAM) to daily precipitation on Antarctica. Our study also shows that Dome Fuji is located in the most influenced region by the SAM. The significant linkage between daily $^{18}O_p$ and the SAM index was extracted at Dome Fuji, located in regions strongly influenced by the asymmetric component of the SAM in the structure of zonal wavenumber 3 and preferred southward flow in SAM^- (Raphael, 2007). As a further study, the investigation of relationships between the major patterns of large-scale circulation (besides the SAM, the Pacific-South American teleconnection patterns and the southern baroclinic annular mode) and $^{18}O_p$ at a daily time scale for other ice core sites of the East Antarctic plateau would determine if our findings for Dome Fuji can be extended to the entire plateau or if differences among the sites exist.

The main driver of the daily $^{18}O_p$ at Dome Fuji in austral summers remains to be investigated, even though their contribution to the annual signals was limited. The seasonal change in the source of the moist air at Dome Fuji was described by (Suzuki et al., 2013): most air parcels came from the ocean during austral winter, while they tended to remain over the ice sheet for more than 5 days during austral summer. The latter corresponds to the post-event pattern precipitation, likely caused by local orographic lifting and radiative cooling as a local phenomenon (Dittman et al., 2016). Our simulation successfully reproduced such an event on 14 December 2003 with a large amount of precipitation. Since SAT in the austral summer was much better simulated than $^{18}O_p$ and precipitation (Figure 1), the representation of clouds and radiation effects might be the keys for the interpretation.

Our results showed the importance of considering the recording processes of isotopic proxies, in linking with atmospheric variability, for the interpretation of water isotope records considering past variations of climate. In this context, future studies should investigate the interpretation of water isotopes in the East Antarctic ice cores for past climates, including the Last Glacial Maximum (LGM), under a model-data approach using isotope-enabled GCMs. LGM has been a major focus for evaluating how well state-of-the-art climate models simulate climate changes as large as those expected in the future using paleoclimate reconstructions (Kageyama et al., 2021). Indeed, the episodic precipitation events may change in seasonality and frequency in different climate states like the LGM, and can also lead to biases in the water isotopes of ice cores (Krinner & Werner, 2003; Noone & Simmonds, 2002; Schlosser et al., 2010; Werner et al., 2016; 2018). In the LGM, paleo-proxies suggested an equatorward shift of the westerly wind in the southern hemisphere (Kohfeld et al., 2013), although many climate models have struggled to reproduce this shift (Sime et al., 2013). Further understanding of the isotope signals using isotope-enabled GCMs may be advantageous to constrain such model-isotope proxy discrepancies.

Acknowledgments, Samples, and Data

- GNIP data are available at https://nucleus.iaea.org/wiser. Ice core data used for Figure S1 are available at https://www.ncdc.noaa.gov/data-access/paleoclimatology-data and are reported in Cauquoin et al. (2019b). SISAL speleothem dataset from Comas-Bru et al. (2019) is available at https://researchdata.reading.ac.uk/256/. Data of a year observation at Dome Fuji is available from the authors of (Fujita & Abe, 2006).
- The code of the isotopic version MIROC5-iso is available upon request on the IIS's GitLab repository (http://isotope.iis.u-tokyo.ac.jp:8000/gitlab/miroc-iso/miroc5-iso, Okazaki and Yoshimura, 2019).
- The source codes and data used in this study are available at https://github.com/kanonundgigue/SAM_DomeFuji and https://doi.org/10.5281/zenodo.4733445.
- The first author is supported by the Japan Society for the Promotion of Science (JSPS) via a Grant-in-Aid for JSPS Fellows. This work was supported by the Japan Society for the Promotion of Science (JSPS) via Grants-in-Aid 17K14397, 19J14488, 19F19024 and JRPs-LEAD with DFG, and the Integrated Research Program for Advancing Climate Models (TOUGOU) Grant Number JPMXD0717935457, ArCS II (Program Grant Number JPMXD1420318865), and DIAS (Grant Number JPMXD0716808979) from the Ministry of Education, Culture, Sports, Science and Technology (MEXT), Japan.
- We also thank Ayako Abe-Ouchi, Koji Fujita, and Masahide Kimoto for their constructive comments.

References

Atsawawaranunt, K., Harrison, S., & Comas-Bru, L. (2019). SISAL (Speleothem

Isotopes Synthesis and AnaLysis Working Group) database version 1b [Data set]. University of Reading. https://doi.org/10.17864/1947.189

Blossey, P. N., Kuang, Z., & Romps, D. M. (2010). Isotopic composition of water in the tropical tropopause layer in cloud-resolving simulations of an idealized tropical circulation: WATER ISOTOPOLOGUES IN THE TTL. *Journal of Geophysical Research*, *115*(D24). https://doi.org/10.1029/2010jd014554

Buizert, C., Gkinis, V., Severinghaus, J. P., He, F., Lecavalier, B. S., Kindler, P., et al. (2014). Greenland temperature response to climate forcing during the last deglaciation. *Science*, *345*(6201), 1177–1180. https://doi.org/10.1126/science.1254961

Buizert, C., Fudge, T. J., Roberts, W. H. G., Steig, E. J., Sherriff-Tadano, S., Ritz, C., et al. (2021). Antarctic surface temperature and elevation during the Last Glacial Maximum. *Science*, *372*(6546), 1097–1101. https://doi.org/10.1126/science.abd2897

Casado, M., Münch, T., & Laepple, T. (2020). Climatic information archived in ice cores: impact of intermittency and diffusion on the recorded isotopic signal in Antarctica. *Climate of the Past*, *16*(4), 1581–1598. https://doi.org/10.5194/cp-16-1581-2020

Cauquoin, A., Landais, A., Raisbeck, G. M., Jouzel, J., Bazin, L., Kageyama, M., et al. (2015). Comparing past accumulation rate reconstructions in East Antarctic ice cores using 10Be, water isotopes and CMIP5-PMIP3 models. *Climate of the Past*, *11*(3), 355–367. https://doi.org/10.5194/cp-11-355-2015

Cauquoin, A., Risi, C., & Vignon, É. (2019). Importance of the advection scheme for the simulation of water isotopes over Antarctica by atmospheric general circulation models: A case study for present-day and Last Glacial Maximum with LMDZ-iso. *Earth and Planetary Science Letters*, *524*, 115731. https://doi.org/10.1016/j.epsl.2019.115731

Cauquoin, A., Werner, M., & Lohmann, G. (2019). Water isotopes – climate relationships for the mid-Holocene and preindustrial period simulated with an isotope-enabled version of MPI-ESM. *Climate of the Past*, *15*(6), 1913–1937. https://doi.org/10.5194/cp-15-1913-2019

Cesana, G., & Chepfer, H. (2012). How well do climate models simulate cloud vertical structure? A comparison between CALIPSO-GOCCP satellite observations and CMIP5 models. *Geophysical Research Letters*, *39*(20). https://doi.org/10.1029/2012gl053153

Chikira, M. (2014). Eastward-Propagating Intraseasonal Oscillation Represented by Chikira–Sugiyama Cumulus Parameterization. Part II: Understanding Moisture Variation under Weak Temperature Gradient Balance. *Journal*

of the Atmospheric Sciences, *71*(2), 615–639. https://doi.org/10.1175/JAS-D-13-038.1

Chikira, M., & Sugiyama, M. (2010). A Cumulus Parameterization with State-Dependent Entrainment Rate. Part I: Description and Sensitivity to Temperature and Humidity Profiles. *Journal of the Atmospheric Sciences*, *67*(7), 2171–2193. https://doi.org/10.1175/2010JAS3316.1

Cole, J. E., Rind, D., Webb, R. S., Jouzel, J., & Healy, R. (1999). Climatic controls on interannual variability of precipitation 18O: Simulated influence of temperature, precipitation amount, and vapor source region. *Journal of Geophysical Research*, *104*(D12), 14223–14235.

Comas-Bru, L., Harrison, S. P., Werner, M., Rehfeld, K., Scroxton, N., Veiga-Pires, C., & SISAL working group members. (2019). Evaluating model outputs using integrated global speleothem records of climate change since the last glacial. *Climate of the Past*, *15*(4), 1557–1579. https://doi.org/10.5194/cp-15-1557-2019

Dahe, Q., Petit, J. R., Jouzel, J., & Stievenard, M. (1994). Distribution of stable isotopes in surface snow along the route of the 1990 International Trans-Antarctica Expedition. *Journal of Glaciology*, *40*(134), 107–118. https://doi.org/10.3189/S0022143000003865

Dansgaard, W. (1964). Stable isotopes in precipitation. *Tell'Us*, *16*(4), 436–468. https://doi.org/10.3402/tellusa.v16i4.8993

Dittmann, A., Schlosser, E., Masson-Delmotte, V., Powers, J. G., Manning, K. W., Werner, M., & Fujita, K. (2016). Precipitation regime and stable isotopes at Dome Fuji, East Antarctica. *Atmospheric Chemistry and Physics*, *16*(11), 6883–6900. https://doi.org/10.5194/acp-16-6883-2016

Dome Fuji Ice Core Project Members, Kawamura, K., Abe-Ouchi, A., Motoyama, H., Ageta, Y., Aoki, S., et al. (2017). State dependence of climatic instability over the past 720,000 years from Antarctic ice cores and climate modeling. *Science Advances*, *3*(2), e1600446. https://doi.org/10.1126/sciadv.1600446

Erb, M. P., Jackson, C. S., Broccoli, A. J., Lea, D. W., Valdes, P. J., Crucifix, M., & DiNezio, P. N. (2018). Model evidence for a seasonal bias in Antarctic ice cores. *Nature Communications*, *9*(1), 1361. https://doi.org/10.1038/s41467-018-03800-0

Federer, B., Brichet, N., & Jouzel, J. (1982). Stable Isotopes in Hailstones. Part I: The Isotopic Cloud Model. *Journal of the Atmospheric Sciences*, *39*(6), 1323–1335. https://doi.org/10.1175/1520-0469(1982)039<1323:SIIHPI>2.0.CO;2

Fischer, H., Severinghaus, J., Brook, E., Wolff, E., Albert, M., Alemany, O., et al. (2013). Where to find 1.5 million yr old ice for the IPICS "Oldest-Ice" ice core. *Climate of the Past*, *9*(6), 2489–2505. https://doi.org/10.5194/cp-9-2489-2013

Fujita, K., & Abe, O. (2006). Stable isotopes in daily precipitation at Dome Fuji, East Antarctica. *Geophysical Research Letters*, *33*(18). https://doi.org/10.1029/2006GL026936

Hirasawa, N., Nakamura, H., & Yamanouchi, T. (2000). Abrupt changes in meteorological conditions observed at an inland Antarctic Station in association with wintertime blocking. *Geophysical Research Letters*, *27*(13), 1911–1914. https://doi.org/10.1029/1999GL011039

Hirasawa, N., Nakamura, H., Motoyama, H., Hayashi, M., & Yamanouchi, T. (2013). The role of synoptic-scale features and advection in prolonged warming and generation of different forms of precipitation at Dome Fuji station, Antarctica, following a prominent blocking event. *Journal of Geophysical Research, D: Atmospheres*, *118*(13), 6916–6928. https://doi.org/10.1002/jgrd.50532

IAEA/WMO. (2018). GNIP. Global Network for Isotopes in Precipitation [Data set]. IAEA: International Atomic Energy Agency/World Meteorological Organization. Retrieved from https://nucleus.iaea.org/wiser

Joussaume, S., & Jouzel, J. (1993). Paleoclimatic tracers: An investigation using an atmospheric general circulation model under ice age conditions: 2. Water isotopes. *Journal of Geophysical Research*, *98*(D2), 2807–2830. https://doi.org/10.1029/92jd01920

Jouzel, J. (1999). GEOSCIENCE:Calibrating the Isotopic Paleothermometer. *Science (New York, N.Y.)*, *286*(5441), 910–911. https://doi.org/10.1126/science.286.5441.910

Jouzel, J., Russell, G. L., Suozzo, R. J., Koster, R. D., White, J. W. C., & Broecker, W. S. (1987). Simulations of the HDO and H 2 18 O atmospheric cycles using the NASA GISS general circulation model: The seasonal cycle for present-day conditions. *Journal of Geophysical Research*, *92*(D12), 14739. https://doi.org/10.1029/JD092iD12p14739

Jouzel, J., Masson-Delmotte, V., Cattani, O., Dreyfus, G., Falourd, S., Hoffmann, G., et al. (2007). Orbital and millennial Antarctic climate variability over the past 800,000 years. *Science*, *317*(5839), 793–796. https://doi.org/10.1126/science.1141038

Kageyama, M., Harrison, S. P., Kapsch, M.-L., Lofverstrom, M., Lora, J. M., Mikolajewicz, U., et al. (2021). The PMIP4 Last Glacial Maximum experiments: preliminary results and comparison with the PMIP3 simulations. *Climate of the Past*, *17*(3), 1065–1089. https://doi.org/10.5194/cp-17-1065-

Kållberg, P., Simmons, A., Uppala, S., & Fuentes, M. (2004). The ERA-40 archive.[Revised October 2007], Shinfield Park. *Reading*, (17). Retrieved from https://www.ecmwf.int/node/10595

Karlsson, N. B., Binder, T., Eagles, G., Helm, V., Pattyn, F., Van Liefferinge, B., & Eisen, O. (2018). Glaciological characteristics in the Dome Fuji region and new assessment for "Oldest Ice'". *Cryosphere*, *12*(7), 2413–2424.

Kohfeld, K. E., Graham, R. M., de Boer, A. M., Sime, L. C., Wolff, E. W., Le Quéré, C., & Bopp, L. (2013). Southern Hemisphere westerly wind changes during the Last Glacial Maximum: paleo-data synthesis. *Quaternary Science Reviews*, *68*, 76–95. https://doi.org/10.1016/j.quascirev.2013.01.017

Krinner, G., & Werner, M. (2003). Impact of precipitation seasonality changes on isotopic signals in polar ice cores: a multi-model analysis. *Earth and Planetary Science Letters*, *216*(4), 525–538. https://doi.org/10.1016/S0012-821X(03)00550-8

Krinner, G., Genthon, C., Li, Z.-X., & Le Van, P. (1997). Studies of the Antarctic climate with a stretched-grid general circulation model. *Journal of Geophysical Research*, *102*(D12), 13731–13745. https://doi.org/10.1029/96jd03356

Laepple, T., Werner, M., & Lohmann, G. (2011). Synchronicity of Antarctic temperatures and local solar insolation on orbital timescales. *Nature*, *471*(7336), 91–94. https://doi.org/10.1038/nature09825

Marshall, G. J., & Thompson, D. W. J. (2016). The signatures of large-scale patterns of atmospheric variability in Antarctic surface temperatures: Antarctic Temperatures. *Journal of Geophysical Research, D: Atmospheres*, *121*(7), 3276–3289. https://doi.org/10.1002/2015JD024665

Marshall, G. J., Di Battista, S., Naik, S. S., & Thamban, M. (2011). Analysis of a regional change in the sign of the SAM--temperature relationship in Antarctica. *Climate Dynamics*, *36*(1), 277–287.

Marshall, G. J., Thompson, D. W. J., & van den Broeke, M. R. (2017). The Signature of Southern Hemisphere Atmospheric Circulation Patterns in Antarctic Precipitation. *Geophysical Research Letters*, *44*(22), 11580–11589. https://doi.org/10.1002/2017GL075998

Masson-Delmotte, V., Kageyama, M., Braconnot, P., Charbit, S., Krinner, G., Ritz, C., et al. (2006). Past and future polar amplification of climate change: climate model intercomparisons and ice-core constraints. *Climate Dynamics*, *27*(4), 437–440. https://doi.org/10.1007/s00382-006-0149-1

Masson-Delmotte, V., Buiron, D., Ekaykin, A., Frezzotti, M., Gallée, H., Jouzel, J., et al. (2011). A comparison of the present and last interglacial periods in six Antarctic ice cores. *Climate of the Past*, *7*(2), 397–423. https://doi.org/10.5194/cp-7-397-2011

Mellor, G. L., & Yamada, T. (1974). A Hierarchy of Turbulence Closure Models for Planetary Boundary Layers. *Journal of the Atmospheric Sciences*, *31*(7), 1791–1806. https://doi.org/10.1175/1520-0469(1974)031<1791:AHOTCM>2.0.CO;2

Mellor, G. L., & Yamada, T. (1982). Development of a turbulence closure model for geophysical fluid problems. *Reviews of Geophysics* , *20*(4), 851. https://doi.org/10.1029/RG020i004p00851

Merlivat, L., & Jouzel, J. (1979). Global climatic interpretation of the deuterium-oxygen 18 relationship for precipitation. *Journal of Geophysical Research*, *84*(C8), 5029. https://doi.org/10.1029/JC084iC08p05029

Nakajima, T., Takamura, T., Yamano, M., Shiobara, M., Yamauchi, T., Goto, R., & Murai, K. (1986). Consistency of aerosol size distributions inferred from measurements of solar radiation and aerosols. *Journal of the Meteorological Society of Japan. Ser. II*, *64*(5), 765–776. https://doi.org/10.2151/jmsj1965.64.5_765

Nakanishi, M. (2001). Improvement of the Mellor–Yamada turbulence closure model based on large-eddy simulation data. *Boundary - Layer Meteorology*, *99*(3), 349–378. https://doi.org/10.1023/a:1018915827400

Nakanishi, M., & Niino, H. (2004). An Improved Mellor–Yamada Level-3 Model with Condensation Physics: Its Design and Verification. *Boundary-Layer Meteorology*, *112*(1), 1–31. https://doi.org/10.1023/B:BOUN.0000020164.04146.98

Noone, D. (2008). The influence of midlatitude and tropical overturning circulation on the isotopic composition of atmospheric water vapor and Antarctic precipitation. *Journal of Geophysical Research*, *113*(D4). https://doi.org/10.1029/2007jd008892

Noone, D., & Simmonds, I. (1998). Implications for the interpretation of ice-core isotope data from analysis of modelled Antarctic precipitation. *Annals of Glaciology*, *27*, 398–402. https://doi.org/10.3189/1998aog27-1-398-402

Noone, D., & Simmonds, I. (2002). Annular variations in moisture transport mechanisms and the abundance of 18O in Antarctic snow. *Journal of Geophysical Research*. Retrieved from https://agupubs.onlinelibrary.wiley.com/doi/abs/10.1029/2002JD002262

Okazaki, A., & Yoshimura, K. (2019). Global Evaluation of Proxy System Models for Stable Water Isotopes With Realistic Atmospheric Forcing.

Journal of Geophysical Research, D: Atmospheres, *124*(16), 8972–8993. https://doi.org/10.1029/2018JD029463

Onogi, K., Tsutsui, J., Koide, H., Sakamoto, M., Kobayashi, S., Hatsushika, H., et al. (2007). The JRA-25 Reanalysis. *Journal of the Meteorological Society of Japan. Ser. II*, *85*(3), 369–432. https://doi.org/10.2151/jmsj.85.369

Raphael, M. N. (2007). The influence of atmospheric zonal wave three on Antarctic sea ice variability. *Journal of Geophysical Research*, *112*(D12). https://doi.org/10.1029/2006jd007852

Rayner, N. A. (2003). Global analyses of sea surface temperature, sea ice, and night marine air temperature since the late nineteenth century. *Journal of Geophysical Research*, *108*(D14). https://doi.org/10.1029/2002jd002670

Satow, K., Watanabe, O., Shoji, H., & Motoyama, H. (1999). The relationship among accumulation rate, stable isotope ratio and surface temperature on the plateau of east Dronning Maud Land, Antarctica. *Polar Meteorology and Glaciology*, *13*, 43–52. https://doi.org/10.15094/00002888

Schlosser, E. (1999). Effects of seasonal variability of accumulation on yearly mean 18O values in Antarctic snow. *Journal of Glaciology*, *45*(151), 463–468. https://doi.org/10.3189/S0022143000001325

Schlosser, E., Manning, K. W., Powers, J. G., Duda, M. G., Birnbaum, G., & Fujita, K. (2010). Characteristics of high-precipitation events in Dronning Maud Land, Antarctica. *Journal of Geophysical Research*, *115*(D14), 3518. https://doi.org/10.1029/2009JD013410

Schlosser, E., Stenni, B., Valt, M., Cagnati, A., Powers, J. G., Manning, K. W., et al. (2016). Precipitation and synoptic regime in two extreme years 2009 and 2010 at Dome C, Antarctica – implications for ice core interpretation. *Atmospheric Chemistry and Physics*, *16*(8), 4757–4770. https://doi.org/10.5194/acp-16-4757-2016

Schlosser, E., Dittmann, A., Stenni, B., Powers, J. G., Manning, K. W., Masson-Delmotte, V., et al. (2017). The influence of the synoptic regime on stable water isotopes in precipitation at Dome C, East Antarctica. *The Cryosphere*, *11*(5), 2345–2361. https://doi.org/10.5194/tc-11-2345-2017

Schneider, D. P., Steig, E. J., & Comiso, J. C. (2004). Recent Climate Variability in Antarctica from Satellite-Derived Temperature Data. *Journal of Climate*, *17*(7), 1569–1583. https://doi.org/10.1175/1520-0442(2004)017<1569:RCVIAF>2.0.CO;2

Schulzweida, U. (2019). *CDO User Guide*. https://doi.org/10.5281/zenodo.3539275

Sekiguchi, M., & Nakajima, T. (2008). A k-distribution-based radiation code and its computational optimization for an atmospheric general circulation model. *Journal of Quantitative Spectroscopy & Radiative Transfer*, *109*(17), 2779–2793. https://doi.org/10.1016/j.jqsrt.2008.07.013

Sime, L. C., & Wolff, E. W. (2011, November 9). Antarctic accumulation seasonality. *Nature*. https://doi.org/10.1038/nature10613

Sime, L. C., Marshall, G. J., Mulvaney, R., & Thomas, E. R. (2009). Interpreting temperature information from ice cores along the Antarctic Peninsula: ERA40 analysis. *Geophysical Research Letters*, *36*(18). https://doi.org/10.1029/2009gl038982

Sime, L. C., Lang, N., Thomas, E. R., Benton, A. K., & Mulvaney, R. (2011). On high-resolution sampling of short ice cores: Dating and temperature information recovery from Antarctic Peninsula virtual cores. *Journal of Geophysical Research*, *116*(D20). https://doi.org/10.1029/2011jd015894

Sime, L. C., Kohfeld, K. E., Le Quéré, C., Wolff, E. W., de Boer, A. M., Graham, R. M., & Bopp, L. (2013). Southern Hemisphere westerly wind changes during the Last Glacial Maximum: model-data comparison. *Quaternary Science Reviews*, *64*, 104–120. https://doi.org/10.1016/j.quascirev.2012.12.008

Sodemann, H., & Stohl, A. (2009). Asymmetries in the moisture origin of Antarctic precipitation. *Geophysical Research Letters*, *36*(22), 149. https://doi.org/10.1029/2009GL040242

Steig, E. J., Grootes, P. M., & Stuiver, M. (1994). Seasonal precipitation timing and ice core records. *Science*, *266*(5192), 1885–1886. https://doi.org/10.1126/science.266.5192.1885

Stenni, B., Scarchilli, C., Masson-Delmotte, V., Schlosser, E., Ciardini, V., Dreossi, G., et al. (2016). Three-year monitoring of stable isotopes of precipitation at Concordia Station, East Antarctica. *The Cryosphere*, *10*(5), 2415–2428. https://doi.org/10.5194/tc-10-2415-2016

Stewart, M. K. (1975). Stable isotope fractionation due to evaporation and isotopic exchange of falling waterdrops: Applications to atmospheric processes and evaporation of lakes. *Journal of Geophysical Research*, *80*(9), 1133–1146. https://doi.org/10.1029/jc080i009p01133

Suzuki, K., Yamanouchi, T., Kawamura, K., & Motoyama, H. (2013). The spatial and seasonal distributions of air-transport origins to the Antarctic based on 5-day backward trajectory analysis. *Polar Science*, *7*(3), 205–213. https://doi.org/10.1016/j.polar.2013.08.001

Takata, K., Emori, S., & Watanabe, T. (2003). Development of the minimal

advanced treatments of surface interaction and runoff. *Global and Planetary Change*, *38*(1), 209–222. https://doi.org/10.1016/S0921-8181(03)00030-4

Taylor, K. E., Stouffer, R. J., & Meehl, G. A. (2012). An Overview of CMIP5 and the Experiment Design. *Bulletin of the American Meteorological Society*, *93*(4), 485–498. https://doi.org/10.1175/BAMS-D-11-00094.1

Thompson, D. W. J., & Woodworth, J. D. (2014). Barotropic and Baroclinic Annular Variability in the Southern Hemisphere. *Journal of the Atmospheric Sciences*, *71*(4), 1480–1493. https://doi.org/10.1175/JAS-D-13-0185.1

Tremaine, D. M., Froelich, P. N., & Wang, Y. (2011). Speleothem calcite farmed in situ: Modern calibration of 18O and 13C paleoclimate proxies in a continuously-monitored natural cave system. *Geochimica et Cosmochimica Acta*, *75*(17), 4929–4950.

Turner, J., Phillips, T., Thamban, M., Rahaman, W., Marshall, G. J., Wille, J. D., et al. (2019). The Dominant Role of Extreme Precipitation Events in Antarctic Snowfall Variability. *Geophysical Research Letters*, *18*, 279. https://doi.org/10.1029/2018GL081517

Watanabe, M., Emori, S., Satoh, M., & Miura, H. (2009). A PDF-based hybrid prognostic cloud scheme for general circulation models. *Climate Dynamics*, *33*(6), 795–816. https://doi.org/10.1007/s00382-008-0489-0

Watanabe, M., Suzuki, T., O'ishi, R., Komuro, Y., Watanabe, S., Emori, S., et al. (2010). Improved Climate Simulation by MIROC5: Mean States, Variability, and Climate Sensitivity. *Journal of Climate*, *23*(23), 6312–6335. https://doi.org/10.1175/2010JCLI3679.1

Werner, M., Heimann, M., & Hoffmann, G. (2001). Isotopic composition and origin of polar precipitation in present and glacial climate simulations. *Tellus. Series B, Chemical and Physical Meteorology*, *53*(1), 53–71. https://doi.org/10.3402/tellusb.v53i1.16539

Werner, M., Haese, B., Xu, X., Zhang, X., Butzin, M., & Lohmann, G. (2016). Glacial–interglacial changes in $H_2{}^{18}O$, HDO and deuterium excess – results from the fully coupled ECHAM5/MPI-OM Earth system model. *Geoscientific Model Development*, *9*(2), 647–670. https://doi.org/10.5194/gmd-9-647-2016

Werner, M., Jouzel, J., Masson-Delmotte, V., & Lohmann, G. (2018). Reconciling glacial Antarctic water stable isotopes with ice sheet topography and the isotopic paleothermometer. *Nature Communications*, *9*(1), 3537. https://doi.org/10.1038/s41467-018-05430-y

Wilson, D. R., & Ballard, S. P. (1999). A microphysically based precipitation scheme for the UK meteorological office unified model. *Quar-*

terly Journal of the Royal Meteorological Society, *125*(557), 1607–1636. https://doi.org/10.1002/qj.49712555707

Yoshimura, K. (2015). Stable Water Isotopes in Climatology, Meteorology, and Hydrology: A Review. *Journal of the Meteorological Society of Japan*, *93*(5), 513–533. https://doi.org/10.2151/jmsj.2015-036

Yoshimura, K., Miyazaki, S., Kanae, S., & Oki, T. (2006). Iso-MATSIRO, a land surface model that incorporates stable water isotopes. *Global and Planetary Change*, *51*(1), 90–107. https://doi.org/10.1016/j.gloplacha.2005.12.007

Yoshimura, K., Kanamitsu, M., Noone, D., & Oki, T. (2008). Historical isotope simulation using Reanalysis atmospheric data. *Journal of Geophysical Research*, *113*(D19), 1299. https://doi.org/10.1029/2008JD010074

Journal of Geophysical Research: Atmospheres

Supporting Information for

Contribution of the Southern Annular Mode to variations in water isotopes of daily precipitation at Dome Fuji, East Antarctica

K. Kino[1,2], A. Okazaki[3], A. Cauquoin[2], and K. Yoshimura[2]

[1]Atmosphere and Ocean Research Institute, The University of Tokyo, Kashiwa, Japan

[2]Institute of Industrial Science, The University of Tokyo, Kashiwa, Japan

[3]Hirosaki University, Hirosaki, Japan

Contents of this file

Introduction

This supporting information provides the following:

(i) Text S1 and Figure S7:

The possible causes of the model-data discrepancy for two precipitation events in austral summer (Figure 2c) are investigated.

(ii) Figure S1:

Different datasets, including isotopic measurements in precipitation, ice cores, and continental speleothems, were used as in Cauquoin et al. (2019b) and compared with the simulation results for global evaluation (Figure S1). The observed $\delta^{18}O_p$ values were obtained from the Global Network for Isotopes in Precipitation (GNIP) observational database for at least five calendar years from 1961 to 2007 (IAEA/WMO, 2018). The ice core data are presented in Table 1 of Cauquoin et al. (2019). $\delta^{18}O$ in the calcite of speleothem was obtained from the Speleothem Isotope Synthesis and Analysis (SISAL) dataset (version 1b: Atsawawaranunt et al., 2019) updated by Comas-Bru et al. (2019). The speleothem values of $\delta^{18}O$ in calcite are converted to $\delta^{18}O$ in drip water as in Cauquoin et al. (2019b) using ERA-40 reanalysis data (Kållberg et al., 2004) and method of Tremaine et al. (2011). The simulated $\delta^{18}O_p$ was in good agreement with present-day observations (Figure S1). The known features of the isotopic effects found by Dansgaard (1964) were well simulated, as confirmed by Okazaki & Yoshimura (2019), namely, enhanced depletion with latitude, altitude, and continentality.

(iii) Figures S2 to S4:

Simulated daily SAT, precipitation, and $\delta^{18}O_p$ were evaluated by comparing the results with the observations of Stenni et al. (2016) in EPICA Dome C from 2008 to 2010.

(iv) Figure S5:

The monthly climatologies of simulated SAT and $\delta^{18}O_p$ at Dome Fuji, with and without weighting by precipitation amount.

(v) Figure S6:

The annual and JJA mean climatologies for simulated vertically integrated $\delta^{18}O_v$ and simulated meridional moisture flux.

(vi) Tables S1 and S2:

Statistical analyses for the simulation results (Table S1) and in-situ observation results at Dome Fuji (Fujita and Abe, 2006; Table S2) were conducted. We used the absolute values because we could not determine the climatology of the observation.

(vii) Table S3:

Same as Table S1 for the entire period of 1981–2010. For SAT and $\delta^{18}O_p$, we used the deviations as described in Section 2.4.

(viii) Table S4:

Standard deviations of modeled daily SAT and $\delta^{18}O_p$ in each month for the entire period of 1981–2010 are also shown in Figure 3.

Text S1.

The precipitation event at the beginning of December 2003 was induced by air intrusion between the ridge and the trough on the continent and the Atlantic ocean, respectively (Figure S7a). Then, the radiative cooling with high pressure expanded toward Dome Fuji (Figure S7b). The moisture inflow around Dome Fuji gave relatively large precipitation with decreasing SAT and $\delta^{18}O_p$ until 4 December (Figure 1), similar to a typical precipitation event during the austral winter. After that day, SAT increased while $\delta^{18}O_p$ was decreasing (Figure 1), suggesting the radiative cooling induced precipitation, and the "precipitation effect" was dominant for $\delta^{18}O_p$. However, only the second half of the simulated feature was confirmed in observation (Figure 1). The low model resolution may induce model-data discrepancies. If the high pressure had expanded toward Dome Fuji before 4 December, it would reduce the overestimation of inflow and accompanying precipitation there.

The overestimation of inflow might also cause the overestimated precipitation event at the beginning of January 2004. The southerly flow-induced this simulated precipitation event (Figure S7c), and the air mass passed over Antarctica then reached Dome Fuji. Because the decreasing trends in simulated SAT and $\delta^{18}O_p$ were comparable to those in observation, the model was supposed to reproduce the dynamical circulation reasonably but may overestimate inflows again.

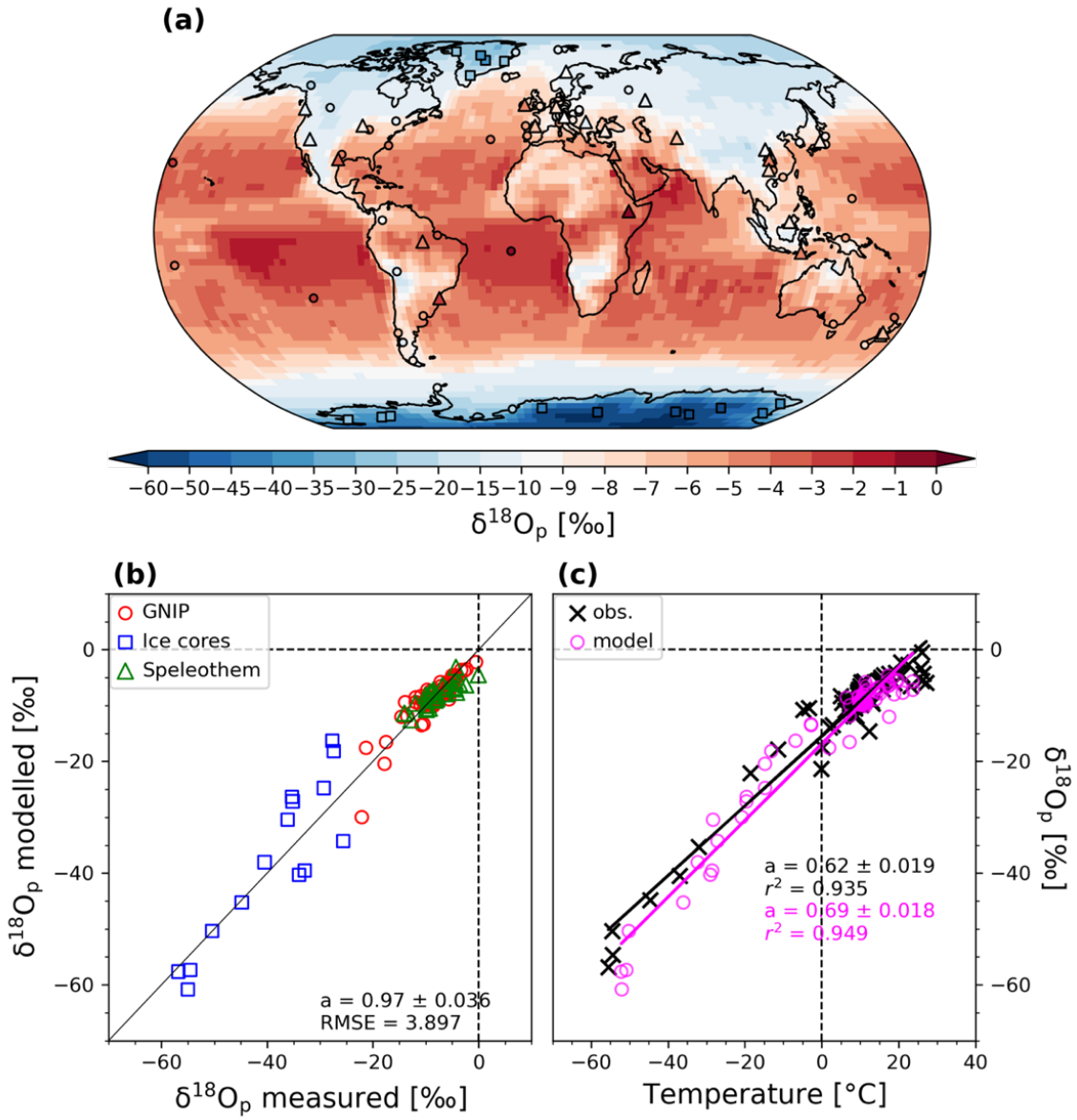

Figure S1. (**a)** Global climatological distribution of simulated (background pattern) and observed (colored markers; see text for details) annual mean $\delta^{18}O$ values in precipitation. The data consist of 70 GNIP stations (circles), 15 ice core records (squares), and 33 speleothem records (triangles). **(b)** Modeled vs. observed annual mean $\delta^{18}O_p$ at the different GNIP, speleothem, and ice core sites. **(c)** Observed (black crosses) and modeled (magenta circles) spatial $\delta^{18}O_p$–surface air temperature relationship. The linear fits for the observed and modeled values are drawn as black and magenta lines, respectively. For **(b)** and **(c)**, the gradients of the linear regression fits are expressed in each panel.

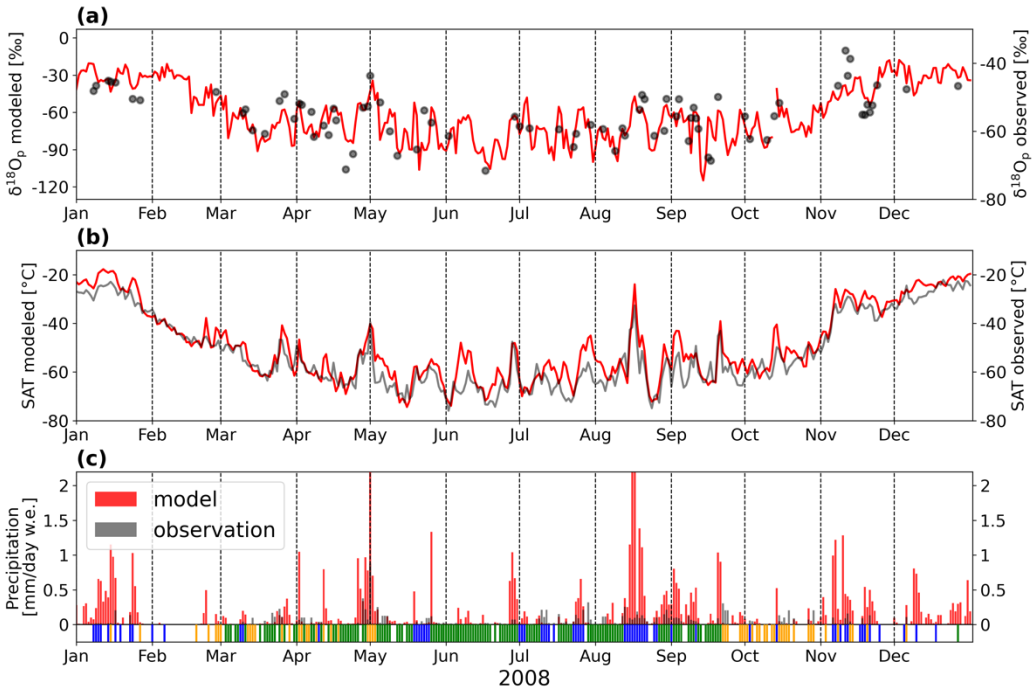

Figure S2. (a) Seasonal changes in simulated (red; left y-axes) and observed (black; right y-axes; Stenni et al., 2016) **(a)** $\delta^{18}O_p$, **(b)** surface air temperature, and **(c)** daily mean precipitation in water equivalent at Dome C for the year 2008. For **(c)**, types of observed precipitation of each day are also shown in the bottom as colored bars: snowfall (yellow), hoar frost (green), diamond dust (blue), and no observation (white).

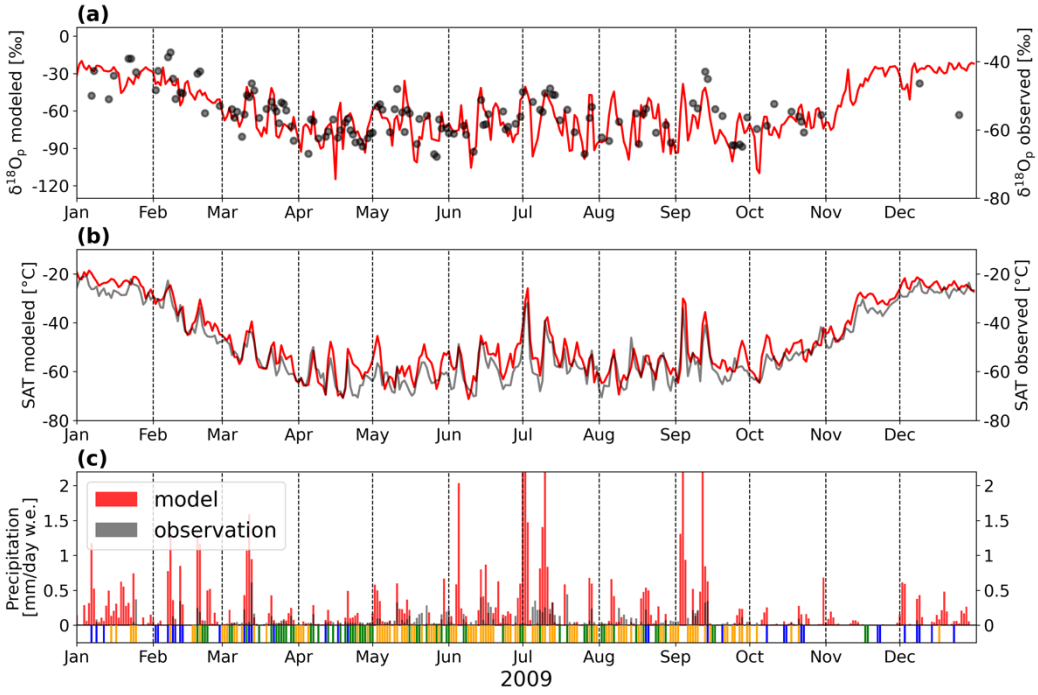

Figure S3. Same as Figure S2 but for 2009.

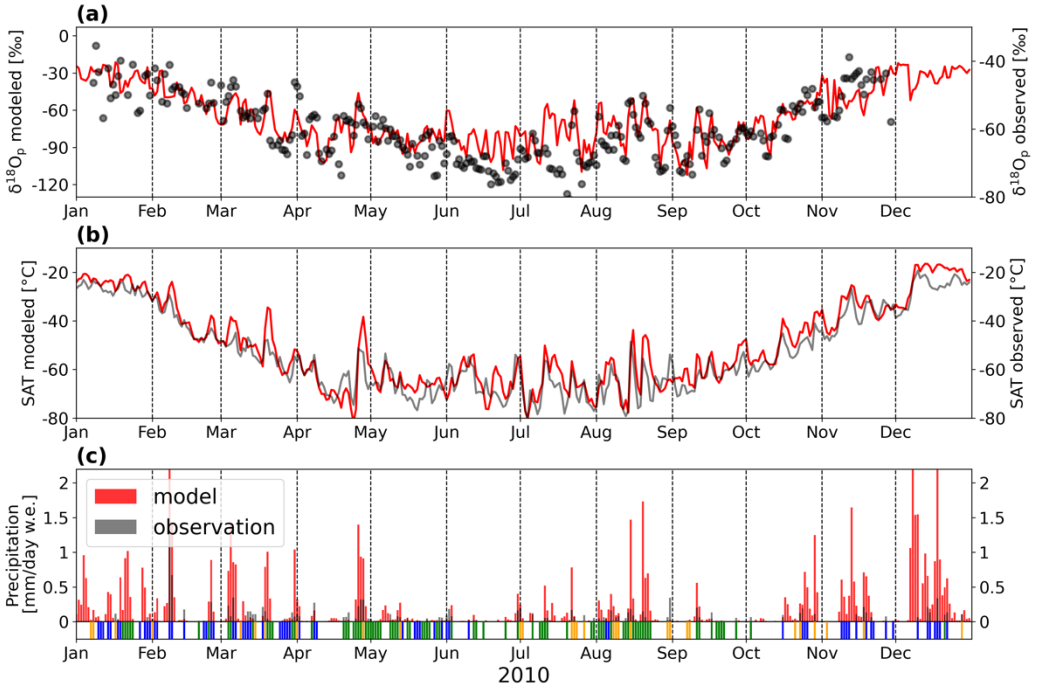

Figure S4. Same as Figure S2 but for 2010.

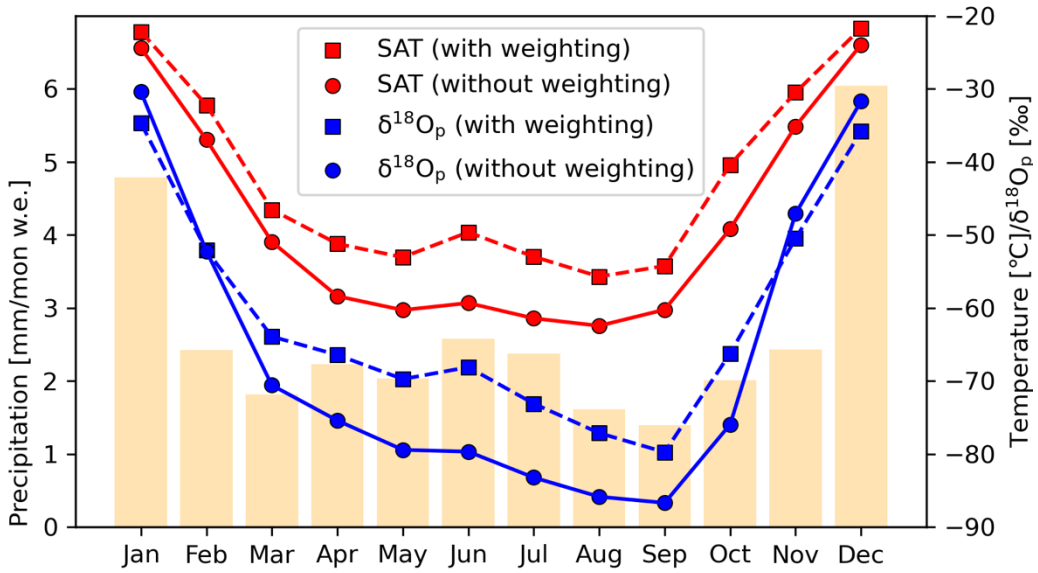

Figure S5. Simulated precipitation (bars; left y-axis), SAT (red; right y-axis), and $\delta^{18}O_p$ (blue; right y-axis) of monthly climatologies. For SAT and $\delta^{18}O_p$, both with and without weighting by precipitation amount are shown by squares with dashed lines and circles with solid lines, respectively. Again, in the legend SAT (with weighting), SAT (no weighting), $\delta^{18}O_p$ (with weighting), $\delta^{18}O_p$ (no weighting).

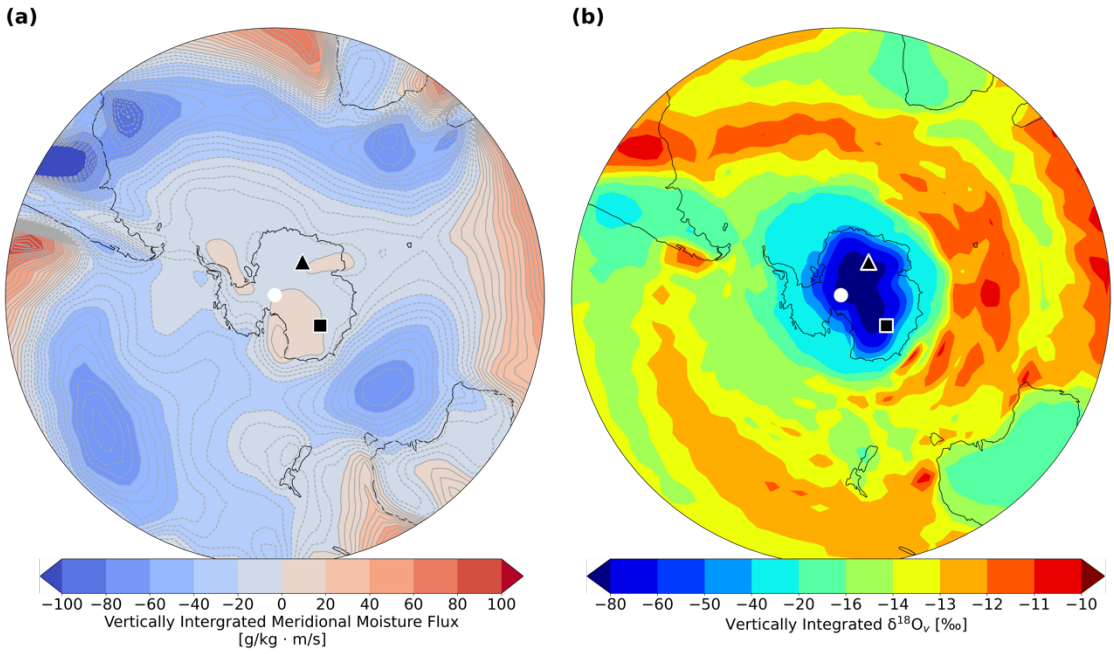

Figure S6. Simulated climatologies in JJA for **(a)** meridional moisture flux and **(b)** vertically integrated $\delta^{18}O_v$. For **(a)**, contours are supplementarily drawn in every 5 g/kg•m/s; northward flux in solid lines; and southward flux in dashed lines. For **(a)** and **(b)**, the location of Dome Fuji and Dome C is plotted as a triangle and square, respectively.

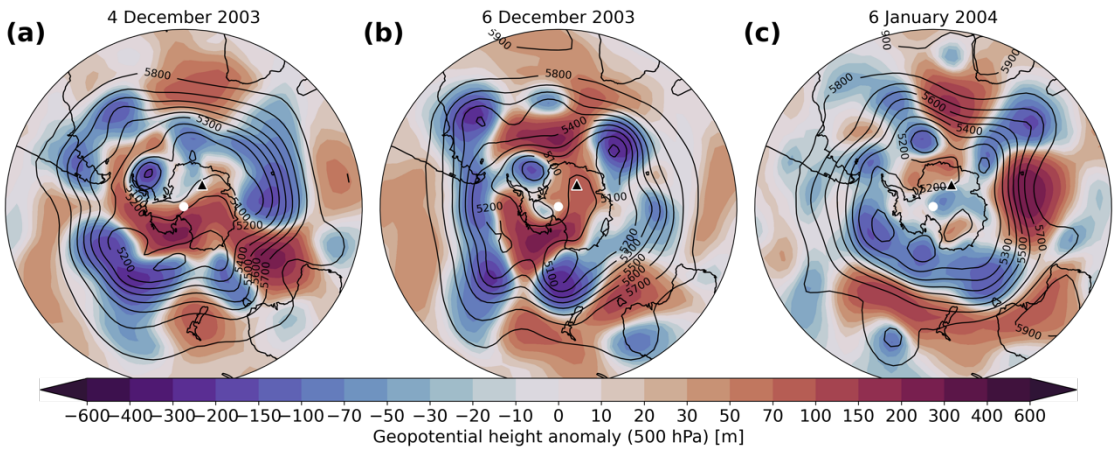

Figure S7. Simulated geopotential height (contours) and its deviation from daily climatology (colors) on **(a)** 4 December 2003; **(b)** 6 December 2003; and **(c)** 6 January 2004. For **(a**–**c)**, the location of Dome Fuji is plotted as a triangle.

	Jan	Feb	Mar	Apr	May	Jun	Jul	Aug	Sep	Oct	Nov	Dec
Number of days	18	23	31	29	31	30	29	31	29	25	26	26
R_{SAT}	NaN	NaN	0.63	0.50	NaN	NaN	0.36	0.57	0.36	0.38	0.37	NaN
p_{SAT}	8.80E-01	9.96E-01	1.54E-04	5.97E-03	7.94E-01	1.04E-01	5.57E-02	8.21E-04	5.39E-02	5.82E-02	6.42E-02	5.96E-01
R_{Pr}	-0.74	NaN	0.50	0.52	NaN	0.58	0.43	0.75	0.41	NaN	NaN	-0.51
p_{Pr}	4.47E-04	5.11E-01	4.08E-03	3.78E-03	6.43E-01	7.72E-04	1.99E-02	1.43E-06	2.70E-02	6.63E-01	1.40E-01	8.11E-03
R_{SAM}	-0.44	0.47	-0.32	0.34	NaN	NaN	-0.60	NaN	NaN	NaN	NaN	NaN
p_{SAM}	6.44E-02	2.32E-02	8.07E-02	7.52E-02	5.98E-01	1.57E-01	6.12E-04	7.40E-01	2.63E-01	5.24E-01	2.71E-01	4.20E-01

Table S1. Spearman's correlation coefficients and p-values between modeled daily $\delta^{18}O_p$, and surface air temperature (R_{SAT} and p_{SAT}), precipitation (R_{Pr} and p_{Pr}), and SAM index (R_{SAM} and p_{SAM}) in each month for the period of the observation (from 3 February 2003 to 20 January 2004). Only correlation coefficients with p-values lower than 0.1 are shown (NaN if not). Only the days with valid values in the simulation and the observation (shown in Table S2) were analyzed. The number of effective days was shown for respective months.

	Jan	Feb	Mar	Apr	May	Jun	Jul	Aug	Sep	Oct	Nov	Dec
Number of days	18	23	31	29	31	30	29	31	29	25	26	26
R_{SAT}	0.65	0.56	0.47	0.40	NaN	0.46	0.60	0.57	0.44	0.51	0.82	0.37
p_{SAT}	3.70E-03	5.94E-03	7.15E-03	3.13E-02	7.66E-01	1.02E-02	5.29E-04	8.83E-04	1.72E-02	9.83E-03	2.92E-07	6.26E-02
R_{Pr}	NaN	NaN	NaN	0.43	0.59	0.77	0.73	0.59	0.46	NaN	0.34	NaN
p_{Pr}	5.02E-01	1.05E-01	5.97E-01	1.97E-02	4.91E-04	5.29E-07	7.17E-06	5.10E-04	1.26E-02	1.30E-01	9.02E-02	3.44E-01
R_{SAM}	NaN	0.39	-0.57	NaN	NaN	NaN	NaN	NaN	-0.51	NaN	-0.57	NaN
p_{SAM}	2.91E-01	6.71E-02	7.54E-04	5.62E-01	6.48E-01	1.26E-01	1.03E-01	1.64E-01	4.82E-03	9.80E-01	2.17E-03	1.35E-01

Table S2. Same as Table S1 but for observation at Dome Fuji (Fujita and Abe, 2006) and the Japanese 25-year reanalysis fields (Onogi et al., 2007).

	Jan	Feb	Mar	Apr	May	Jun	Jul	Aug	Sep	Oct	Nov	Dec
Number of days	930	847	930	900	930	900	930	930	896	858	893	930
R_{SAT}	-0.27	0.15	0.44	0.41	0.45	0.54	0.54	0.48	0.43	0.44	NaN	-0.18
p_{SAT}	9.31E-17	8.60E-06	1.36E-44	7.50E-37	1.17E-47	1.15E-69	1.30E-72	4.35E-55	1.20E-41	1.18E-42	8.53E-02	1.45E-08
R_{Pr}	-0.52	-0.18	0.43	0.56	0.46	0.49	0.46	0.42	0.46	0.29	-0.37	-0.55
p_{Pr}	3.48E-64	8.81E-08	1.31E-42	3.99E-76	5.10E-51	2.25E-56	9.22E-51	1.10E-41	8.14E-49	1.52E-18	1.17E-29	4.56E-75
R_{SAM}	NaN	-0.11	-0.18	-0.16	-0.28	-0.35	-0.49	-0.39	-0.33	-0.34	-0.24	-0.10
p_{SAM}	8.85E-02	9.43E-04	7.20E-08	1.43E-06	1.30E-17	4.23E-28	1.91E-57	4.91E-36	4.71E-24	1.74E-25	1.23E-13	2.05E-03

Table S3. Spearman's correlation coefficients and p-values between modeled daily $\delta^{18}O_p$ and SAT (R_{SAT} and p_{SAT}), precipitation (R_{Pr} and p_{Pr}), and SAM index (R_{SAM} and p_{SAM}) in each month. For $\delta^{18}O_p$ and SAT, deviations from daily climatology for the entire period of 1981–2010 were used, as described in Section 2.4. Only correlation coefficients with p-values lower than 0.05 are shown (NaN if not). The number of effective days used for the analysis was also shown for respective months.

	Jan	Feb	Mar	Apr	May	Jun	Jul	Aug	Sep	Oct	Nov	Dec
SAT [°C]	2.77	4.49	5.72	6.86	8.24	8.45	8.57	7.41	6.97	6.21	4.51	2.77
$\delta^{18}O_p$ [‰]	6.62	8.34	9.28	10.50	12.29	12.18	13.33	12.31	12.25	13.57	9.47	6.82

Table S4. Standard deviations of modeled daily SAT and $\delta^{18}O_p$ in each month. Deviations from daily climatology for the entire period of 1981–2010 were used for each variable, as described in Section 2.4.